Correspondence to:
A. R. Jacobson,
abramj@u.washington.edu

A method to estimate whistler wave vector from polarization using three-component electric field data

Abram R. Jacobson[1], Robert H. Holzworth[1], Robert Pfaff[2], Roderick Heelis[3], and Patrick Colestock[4]

[1]Earth and Space Sciences Department, University of Washington, Seattle, Washington, USA, [2]NASA Goddard Spaceflight Center, Greenbelt, Maryland, USA, [3]Center for Space Sciences, University of Texas at Dallas, Richardson, Texas, USA, [4]ISR-1, Los Alamos National Laboratory, Los Alamos, New Mexico, USA

Abstract Satellites in the Earth's magnetosphere can be used to record the rich electromagnetic wave activity due to terrestrial lightning, typically up to several tens of kilohertz. With simultaneous recordings of the three components of wave electric field E and of the three components of wave magnetic field B, the entire wavefield, polarization, and wave vector can be specified without any appeal to a priori assumptions about the wave mode and without any reliance on the validity of a dispersion relation. However, some satellites lack such a complete suite of measurements. We develop a method which assumes the theoretical dispersion relation for whistler waves then uses recordings of the three components of wave electric field E but no magnetic components to derive the wave polarization and the wave vector (up to a sign ambiguity on the latter). The method can work only because the dispersion relation, which is assumed, already contains information from the full Maxwell's equations. We illustrate the method with 12 s duration simultaneous recordings, at 32 kilosample/s, of three orthogonal components of wave electric field E from the C/NOFS satellite in low-Earth orbit. Our particular example in this article is shown to contain two broadband whistler features in the range of 4–15 kHz, whose wave vectors differ both according to their polar angles from the geomagnetic field B_0 and according to their azimuth around the geomagnetic field B_0.

1. Introduction

For over half century, satellites in the Earth's magnetosphere have provided essential in situ observations of the propagation of whistlers [for an early review, see *Helliwell*, 2006, section 7.3] and other wave modes in the Earth's magnetoplasma. More recently, some satellites, e.g., INTERBALL 2 [*Santolik et al.*, 2003] and DEMETER [*Berthelier et al.*, 2006; *Chum et al.*, 2009; *Parrot et al.*, 2008], have provided simultaneous recordings, in the ELF and VLF (extremely and very low frequency, 0.3–3 and 3–30 kHz), of three components of the wave electric field E plus three components of the wave magnetic field B. These full "multicomponent" data suites allow complete reconstruction of the wavefield in portions of the ELF/VLF, including the wave polarization and the wave vector's unambiguous orientation and magnitude [*Santolik et al.*, 2003]. This complete reconstruction allows discrimination between the modes of propagation predicted by the WKB theory (an excellent recapitulation of Stix is in *Gurnett et al.* [1965]; see also *Stix* [1962]). An example of two modes of propagation involves the (mostly electromagnetic) electron whistler versus the (mostly electrostatic) lower hybrid wave [*Bell and Ngo*, 1988; *Bell and Ngo*, 1990]. A single-antenna recording of an electric field component cannot discriminate between these two modes, which differ widely in dispersion, phase velocity, group velocity, and polarization. Only with the polarization and the wave vector can a signal be properly interpreted. In addition, the wave vector furnishes the initial condition for a numerical backward raytrace (from the satellite) [*Chum et al.*, 2009; *Santolik et al.*, 2009, 2003]. Without a specified starting value of the wave vector, the raytrace is arbitrary and can furnish neither a unique raypath estimate nor useful guidance on the source region of the wave. The source region would add important information on the origin of the observed wavefields.

This article describes a method to characterize the polarization and to infer the wave vector from incomplete data, e.g., three components of wave E but lacking any components of wave B. These three components on their own are inadequate to discriminate the mode of propagation or to specify the wave vector. However, assuming the dispersion relation, one can enlist more information on the observed wave, as the dispersion relation
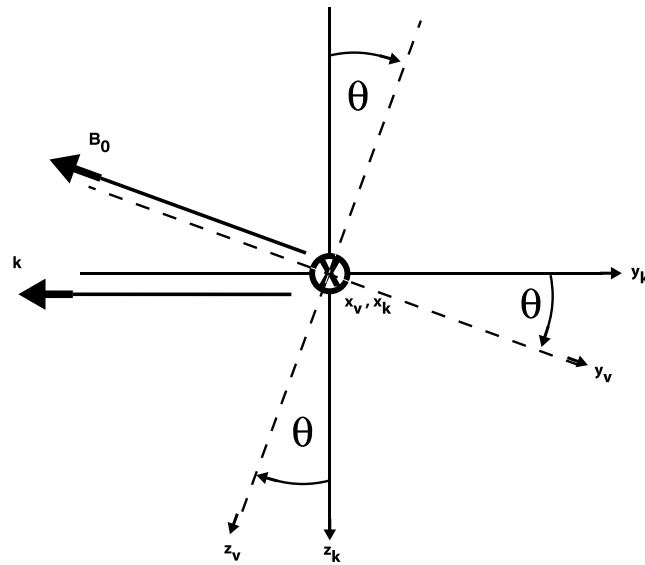
Figure 1. View of the k, B_0 plane containing the wave vector k and the geomagnetic field B_0. The angle between these two vectors is θ. Two coordinate systems are defined, (x_k, y_k, and z_k) are tied to k and (x_v, y_v, and z_v) are tied to B_0. The vector k lies along the $-y_k$ direction, while B_0 lies along the $-y_v$ direction. The x_v and x_k axes coincide and are pointed into the plane of the diagram.

[see *Gurnett et al.*, 1965, equation (12) et seq] is based on the entire set of Maxwell's equations. In this manner, we will infer the wave vector, although with a discrete sign ambiguity.

There was an earlier technique [*Means*, 1972] which used a covariance matrix approach to retrieve the wave polarization and wave vector from three orthogonal magnetic sensors from the OGO 6 spacecraft. The wave studied in the article's example was a proton whistler in the ELF band. The method's computation of a covariance matrix using the three signals was done over the entire signal passband at one time, rather than, as in the method we present below, frequency by frequency in the Fourier domain.

We will illustrate the method we have developed with burst-mode recordings of three components of E [*Jacobson et al.*, 2011] by the Vector Electric Field Instrument (VEFI) payload [*Pfaff et al.*, 2010] on the C/NOFS satellite [*de La Beaujardiere*, 2004]. The VEFI provides burst-mode recordings of all the three components of wave E (but without wave B) at a sampling rate of ~32 kilosample/s (kS/s), allowing a Nyquist frequency of 16 kHz. This provides an excellent coverage of the ELF/VLF emissions from lightning, which is our main interest in the current work. C/NOFS' lack of simultaneous burst-mode recordings of wave B, at the same high sample rate of 32 kS/s, motivated our development of an alternative method for inferring the full wavefield from E alone, even if with residual sign ambiguities.

2. Method to Infer Orientation of Wave Vector From Three-Component Recordings of Wave Electric Field

2.1. Symmetry and Principal Axes

"Wave polarization" describes the phase and amplitude relationships between the two orthogonal components of the wave electric field within the plane of constant phase, that is within the plane whose normal is the wave vector k [*Stix*, 1962]. It has been known for a half century that if we neglect collisions, VLF whistler waves in the inner magnetosphere should be right-hand elliptically polarized in the plane of constant phase [*Gurnett et al.*, 1965; *Stix*, 1962]. The whistler polarization in the quasi-longitudinal approximation becomes purely right-hand circular if ion effects are ignored [see *Helliwell*, 2006, equation (3)]. The definition of "right" or "left" sense is actually controlled by the magnetic field orientation, not by k. Right means corotating with electrons, while left means corotating with ions. This definition is convenient in that the physics, rather than in that the magnetic hemisphere, controls the polarization.

The "k, B_0" plane containing both the wave vector k and the geomagnetic field B_0 is shown in Figure 1. The angle between k and B_0 is θ. Two coordinate systems are shown: The "k" coordinate systems (x_k, y_k, and z_k) are tied to k, which is directed in the $-y_k$ direction. The "v" coordinate systems (x_v, y_v, and z_v) are tied to B_0, which is directed in the $-y_v$ direction. Both x_k and x_v coincide and are directed into the page. This direction is the intersection of two planes: with the plane (x_k, z_k) whose normal is k and with the plane (x_v, z_v) whose normal is B_0.

The only symmetry breaker in the index of refraction is that B_0 is not parallel to k (except in the extreme limit $\theta = 0$). This means that in the plane whose normal is k, in which the polarization is defined, the polarization ellipse principal axes must coincide with the axes (x_k and z_k). That is, one principal axis must be in the k, B_0 plane and normal to k (that is, must be along z_k), while the other principal axis must be normal to the k, B_0
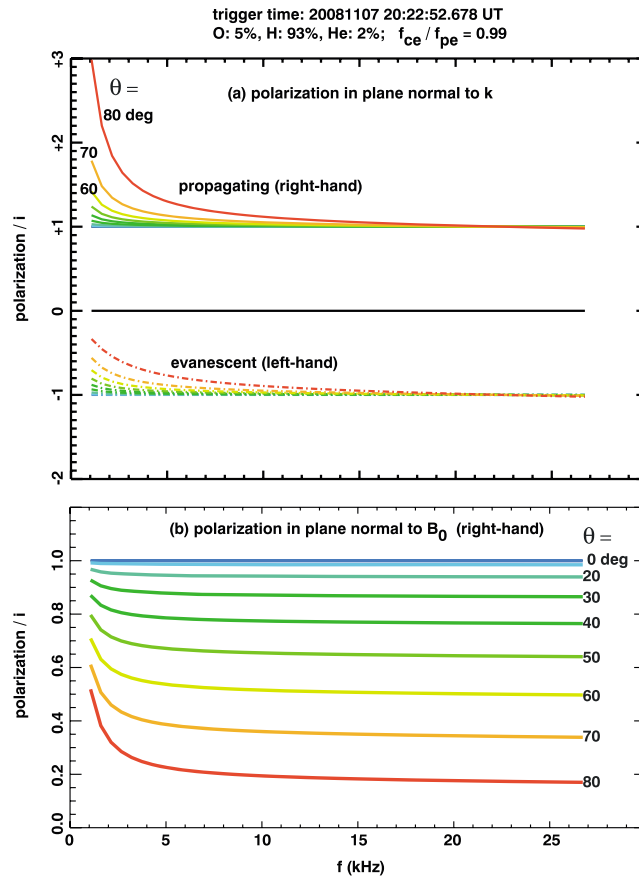
Figure 2. (a) Theoretical polarization, defined as E_{xk}/E_{zk}, in the plane normal to k. The polarization is purely imaginary. The solid curves are for the propagating right-hand polarized (whistler) mode. The dashed curves are for the evanescent left-hand polarized mode. The different colors are for steps in θ, from 0° (blue) to 80° (red) in steps of 10°. The ion effects account for the noncircularity at the low frequencies and are based on the CINDI measurements of ion composition (see heading). (b) Polarization transferred to the plane normal to B_0, using equation (9).

plane (that is, must be along x_k). The wave polarization [*Gurnett et al.*, 1965; *Stix*, 1962] is defined as the ratio of the wave electric field normal to the k, B_0 plane over the wave electric field in that plane and normal to k:

$$\rho \equiv \frac{\boldsymbol{E} \cdot \boldsymbol{x_k}}{\boldsymbol{E} \cdot \boldsymbol{z_k}}. \qquad (1)$$

2.2. Predicted Polarization

We now illustrate the predicted polarization for a typical C/NOFS instance, at approximately 20:22:53 UT on 7 November 2008. The satellite was at altitude 598 km, longitude 99.76°E, and latitude −11.26°N. The electron gyrofrequency was $f_{ce} = 981$ kHz. The ion composition is given by the Coupled Ion-Neutral Dynamics Investigation (CINDI) [*Heelis et al.*, 2009] payload on C/NOFS. The oxygen-, hydrogen-, and helium-ion percentages for this instance are ~O^+ 5%, H^+ 93%, and He^+ 2%. Figure 2a graphs the predicted polarization [see *Gurnett et al.*, 1965, equation (16)] for these ion abundances and for the electron cyclotron frequency to electron plasma frequency ratio $f_{ce}/f_{pe} = 0.99$. The set of solid curves in Figure 2a is for the propagating, right-hand elliptical whistler solution. The set of dashed curves in Figure 2a is for the evanescent, left-hand elliptical solution. Color indicates θ (see Figure 1) in 10°

increments, with red = 80°, amber = 70°, yellow = 60°, etc down to blue = 0°. The effect of ions is greatest at the lower frequencies, approaching the ion cyclotron resonances, and is greatest when k approaches orthogonality to B_0, that is when θ (see Figure 1) approaches 90°.

2.3. Transforming Polarization to the Plane Normal to B_0

The VEFI payload takes simultaneous burst-mode recordings of three orthogonal components of the wave electric field. These three measurements in the VEFI burst mode are not enough to determine either the wave vector or the Poynting vector, determination of which would require that the suite of recordings also include at least two components of the wave magnetic field too [*Chum et al.*, 2009; *Santolik et al.*, 2003]. Therefore, we cannot infer the orientation of k from the VEFI burst-mode measurements, resulting in our being unable to directly infer the wave polarization. The only plane that we can use in a first-pass analysis is the plane we actually know, i.e the plane normal to B_0, which differs, except for the extreme limit θ = 0, from the plane normal to k.

Nonetheless, combining the theoretical polarization in the plane normal to k [*Gurnett et al.*, 1965] with the recordings of all the three components of the wave electric field, we can infer key information on the orientation of k. This step does not appear to have been reported previously in the literature, as far as we can tell. Instead, the satellites with complete "multicomponent" recordings (three components of wave E plus three components of wave B) have directly retrieved both the wave vector orientation and the Poynting vector (see, for example, the work with DEMETER in *Chum et al.*[2009]). We will show that by assuming the

theoretical whistler polarization, we can use our three components of wave E to infer the orientation of k, albeit with a sign ambiguity.

The two components of wave electric E in the plane normal to k are E_{zk} and E_{xk}. The component E_{zk} has a nonzero projection onto B_0 except in the extreme limit $\theta = 0$. That projection is $-E_{zk} \sin(\theta)$ (see Figure 1). On the other hand, for very low frequencies in the inner magnetosphere, where $f << f_{ce}$ and $f << f_{pe}$, electron mobility effectively suppresses the electric field along B_0, so that there must be a field component E_{yk} antiparallel to k to ensure zero field along B_0. Thus, from Figure 1, we have to a very good approximation

$$-E_{zk} \sin(\theta) - E_{yk} \cos(\theta) = 0. \tag{2}$$

so that the required electric field antiparallel to k is

$$E_{yk} = -E_{zk} \tan(\theta). \tag{3}$$

as shown elsewhere [see *Helliwell*, 2006, equation (3)]. We define the polarization ρ_k in the plane normal to k as the ratio of the field normal to the k, B_0 plane, to the field normal to k, and lying in the k, B_0 plane:

$$\rho_k = E_{xk} \; / \; E_{zk}. \tag{4}$$

The wave electric field in the plane normal to B_0 and in the k, B_0 plane is

$$E_{zv} = E_{zk} \cos(\theta) - E_{yk} \sin(\theta). \tag{5}$$

Substituting equation (3) into equation (5), we get

$$E_{zv} = E_{zk} \cos(\theta) + E_{zk} \sin(\theta) \tan(\theta).$$

$$E_{zv} = \left[E_{zk} / \cos(\theta) \right] \left(\cos^2(\theta) + \sin(\theta)^2 \right) = E_{zk} / \cos(\theta). \tag{6}$$

It is worth noting that equation (6) is not dependent on propagation mode but rather is just a consequence of the requirement that the wave E must vanish parallel to B_0. We define the polarization ρ_b in the plane normal to B_0 as the ratio of the field normal to the k, B_0 plane, to the field normal to B_0, and lying in the k, B_0 plane:

$$\rho_b = E_{xv} \; / \; E_{zv}. \tag{7}$$

Since $E_{xv} = E_{xk}$ (see Figure 1), substituting equation (6) into equation (7) gives

$$\rho_b = \rho_k \cos(\theta). \tag{8}$$

This counterintuitive result is entirely due to the nonzero wave electric field along k required to ensure zero electric field along B_0. Where there is no such wave electric field along k, we would naively expect (equation (5)) that the polarization in the plane normal to B_0 would be $\rho_k / \cos(\theta)$. This naive result is a simple foreshortening of z_k projected onto z_v. For the x_k axis, there is no foreshortening into x_v, as they are one and the same (see Figure 1). Hence, without the wave electric field along k required to ensure zero electric field along B_0, we would expect $\rho_k < \rho_b$. The counterintuitive result in equation (8) however is that due to the required nonzero wave electric field along k, we get $\rho_k > \rho_b$, so that the ellipse major axis is aligned with the k, B_0 plane's intersection with the plane normal to B_0.

Figure 2b shows the polarization (divided by i) in the plane normal to B_0, for each of the nine values of θ, from 0° (blue) to 80° (red), in 10° steps. We also (not shown) calculate a denser and wider set of 90 such curves of polarization versus frequency, for 90 values θ, from 0° to 89°, in 1° steps. We will use this matrix to interpolate θ from the measured ellipse aspect ratio.

Figure 3 illustrates schematically how the polarization ellipse transforms between the two planes in which it may be defined. Figure 3a shows the plane normal to k. The approximately circular polarization ellipse is shown as a solid curve. The dashed line is the intersection of the plane with the k, B_0 plane. Figure 3b shows the plane normal to B_0, with the axes rotated to use e, magnetic east zonal, as one axis, and m, magnetic inward meridional, as the other axis normal to B_0. (Full details are provided in the Appendix.) The e and m axes have direct geophysical significance, unlike coordinates tied to the satellite. Transformations
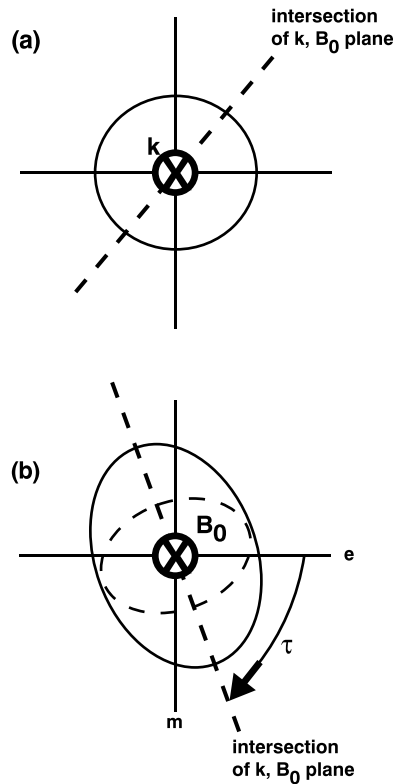
Figure 3. Cartoon of the polarization in the plane normal to (a) the wave vector k, as conventionally defined, and to (b) the geomagnetic field B_0. The intersections of the k, B_0 plane with (Figure 3a) the plane normal to k and with (Figure 3b) the plane normal to B_0 are shown as dashed lines. The polarization in Figure 3a, the plane normal to k, is pictured as circular in this argument, for simplicity. If the only effect in transforming polarization from the plane normal to k to the plane normal to B_0 was geometrical foreshortening, then the inner ellipse in Figure 3b would represent the polarization in the plane normal to B_0. However, the effect of the space charge electric field along k is to invert the polarization (solid ellipse) in the plane normal to B_0 relative to the foreshortening effect. The axes in Figure 3b, the plane normal to B_0, are labeled "e" for magnetic zonal east and "m" for magnetic meridional inward. The major axis of the polarization ellipse is tilted by angle τ from the e axis toward the m axis.

from satellite to e and m coordinates are given in the Appendix. Again, the dashed line in Figure 3b is the intersection of the plane with the k, B_0 plane. The dashed ellipse in Figure 3b indicates the naively expected polarization ellipse based on the (wrong) assumption of zero electric field along k. The solid ellipse shows the true polarization in the plane normal to B_0; the ellipse has been elongated along the inter-section axis due to the contribution of a nonzero electric field along k.

2.4. Application to Direction Finding of Wave Vector k

The polarization result allows us to infer the azimuth of the k, B_0 plane about B_0. We note from Figure 2 that the wave polarization ρ_k in the plane normal to the wave vector is close to and at lower frequencies greater than $\rho_{k\sim+i}$. In the plane normal to the geomagnetic field, the polarization ellipse major axis will be along the azimuth of the k, B_0 plane. This is the azimuth of the projection of k onto the plane normal to the geomagnetic field. Moreover, we can retrieve θ from the measured ratio of minor-to-major axis, as indicated in the discussion of Figure 2b. Formally, from equation (8) above,

$$\theta = \cos^{-1}\left(\rho_b / \rho_k\right). \qquad (9)$$

We note that the inferred direction of k will be fourfold ambiguous: First, τ is indistinguishable from $\tau + 180°$. Second, θ is indistinguishable from $180° - \theta$. This direction finding ambiguity is an inevitable consequence of our having simultaneous measurements of only the three components of wave E without any measurements of wave B. Some of that ambiguity can be eliminated by situational context on a case-by-case basis, but that is not guaranteed. This problem is not shared by a more complete suite of measurements, such as that available at 1.25 kHz and below on the DEMETER satellite [*Chum et al.*, 2009; note that the underlying parameter retrieval method for complete multicomponent data is given by *Santolik et al.* [2003].

However, this problem of the present treatment is in practice not very important, as the spectral dispersion substantially discriminates between the "upgoing" and "downgoing" possibilities.

3. Illustration of the Method With VEFI Data

3.1. The C/NOFS Satellite and VEFI Instrument

The C/NOFS satellite [*de La Beaujardiere*, 2004] carries the Vector Electric Field Instrument payload [*Pfaff et al.*, 2010]. The C/NOFS orbit is very low inclination (~13°) and slightly elliptical (perigee ~ 400 km, apogee ~ 850 km). The VEFI contains three orthogonal antenna pairs to measure the electric field, from DC through very low frequency. Each antenna pair extends ~20 m tip to tip. The Appendix presents geometrical transformations from satellite coordinates to geophysically meaningful coordinates e and m in the plane normal to the Earth's magnetic field. An earlier publication [*Jacobson et al.*, 2011] used a single VEFI antenna's burst-mode data, in which the sampling rate is ~32 kS/s and the Nyquist frequency is ~16 kHz. In what follows, we treat all the three orthogonal components of wave E, which are simultaneously sampled at ~32 kS/s and stored.

Although C/NOFS' mission is primarily related both to equatorial plasma irregularities [*de La Beaujardiere*, 2004] and to the background conditions that are predictive of irregularity growth [*Pfaff et al.*, 2010], the VEFI burst-mode data recordings frequently occur in "quiet" conditions characterized by smooth and unperturbed electron density. The examples featured below are all from quiet conditions. This allows the basic features of whistler wave polarization to be viewed in a "simple" setting, without the complication of scattering off of plasma irregularities into quasi-electrostatic lower hybrid waves [*Bell and Ngo*, 1988, 1990]. The latter form of scattering is a prominent feature of the VEFI recordings if even moderate irregularities are present, but the data selected here are chosen to avoid that complication.

The epoch chosen for the example is a 12 s recording of three orthogonal electric field components (see Appendix). The satellite was at altitude 598 km, longitude 99.76°E, and latitude −11.26°N, on an *L* shell $L = 1.24$. The electron gyrofrequency is $f_{ce} = 981$ kHz. The ion composition, given by the CINDI [*Heelis et al.*, 2009] payload on C/NOFS, is ~O^+ 5%, H^+ 93%, and He^+ 2%, as was noted in Figure 2 above. The magnetic inclination at the satellite was −41.2°.

3.2. Observations From the Entire 12 s Recording

Figure 4 presents moving window spectrograms for the same recording epoch as was chosen for Figure 2 above. The Fourier transform window is 256 samples wide, and it is advanced by 1/16 of the window width. The color scale is logarithmic in the spectral density. The components in Figure 4 have been transformed into geophysical coordinates and are (Figures 4a and 4d) magnetic zonal east, along *e*; (Figures 4b and 4e) magnetic meridional inward, along *m*; and (Figure 4c) parallel to the Earth's magnetic field B_0 at the satellite. The last component is included as a "sanity check": We have assumed that this component is vanishingly small, but we can check that assumption with our data. For the 12 s recording shown in this example, we confirm that the mean square electric field parallel to B_0 is only 0.0017 of the mean square electric field perpendicular to B_0. Given inevitable errors in the satellite attitude, in the antenna boom orientations, and in the International Geomagnetic Reference Field (IGRF) magnetic field specification, this 0.0017 ratio gives us confidence that the entire "end-to-end" alignment is adequately characterized and permits the polarization analysis to follow.

Figure 4 indicates a complex and varied mixture of wave signatures during the 12 s example. The most intense, though also the briefest, wave signatures are the minimally dispersed broadband impulses extending over most of the passband. These are "fractional hop" signals that have entered the ionosphere from the Earth-ionosphere waveguide (a good review of the EIWG is given by *Cummer* [2000]) and then propagated only up through the ionosphere to the satellite [see *Helliwell*, 2006, Table 4-1, "Whistler Types"]. The weak dispersion of the fractional hop features identifies that they have neither transited from the conjugate ionosphere nor been ducted by repeated reflections from the protonosphere as "subprotonospheric whistlers" [*Barrington and Belrose*, 1963; *Carpenter et al.*, 1964; *Smith*, 1965].

In addition to the broadband fractional hop whistlers, Figure 4 shows more diffuse features mainly in the frequency range 1–5 kHz. The clearest example of the diffuse features occurs in the times 6–10 s in Figure 4b. Three seconds of this feature are shown in detailed spectrograms for (Figure 4d) the magnetic zonal east and (Figure 4e) the magnetic meridional inward components of the electric field. The diffuse feature is much stronger on the magnetic meridional than the magnetic zonal component. This shows that the diffuse feature's polarization ellipse must be eccentric with the major axis close to the *m* direction (see Figure 3b above). The width and dispersion of these diffuse features is similar to those of the DEMETER observations [see *Chum et al.*, 2009, Figure 2] of subprotonospheric whistlers. The width, dispersion, and spectral extent are also similar to those parameters seen in the original rocket and satellite observations [see *Carpenter et al.*, 1964, Figures 2, 4, and 5].

In addition to the two forms of whistlers mentioned above, there is a very dispersed, diffuse feature that is present in the first 4 s of the recording. Like the suspected subprotonospheric echoes, this highly dispersed feature is brighter along the *m* than along the *e* axis, indicating a polarization major axis nearly in the magnetic meridian.

Figure 4 might give the impression that most of the lightning signals are a structureless blur. However, the impression is just an artifact of the extreme demagnification of this figure. Later, we will show how a finer-scale view of the lightning signals reveals that they are a myriad of quasi-discrete waveforms, usually not blurred together.
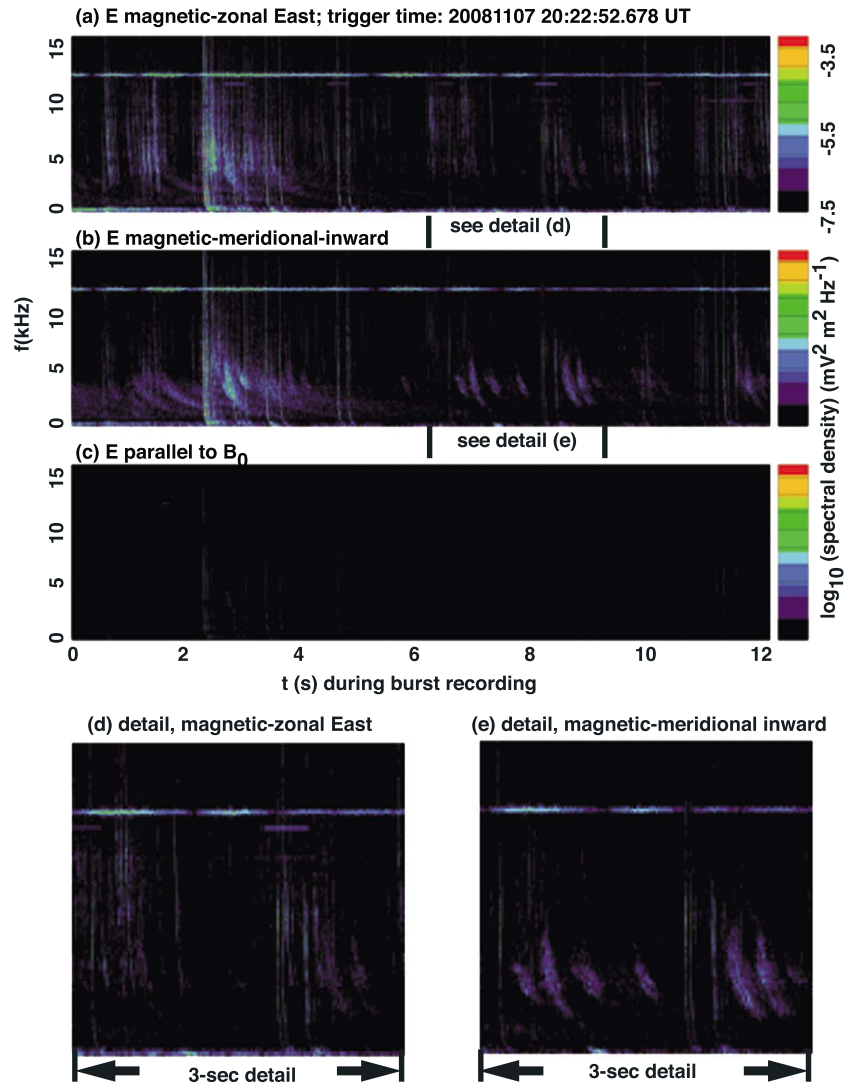
Figure 4. Spectrograms of wave electric field along directions (a and d) magnetic zonal eastward, (b and e) magnetic meridional inward, and (c) parallel to B_0 during the entire 12 s record. A 3 s detail of Figure 4a is shown in Figure 4d, and a 3 s detail of Figure 4b is shown in Figure 4e. The Fourier window is 256 samples long and is advanced by 1/16 of its width. The color scale is logarithmic and is identical for all the panels (Figures 4a–4e).

Customarily, the angle ε is used to quantify the axial ratio (minor axis/major axis) of the polarization ellipse [*Shao and Jacobson*, 2001]: aspect ratio $=\tan(\varepsilon)$. See Appendix for details. The angle ε can take values only from $-45°$ (left-hand circular) to $+45°$ (right-hand circular). Linear polarization is given by $\varepsilon = 0°$, left-hand elliptical by $-45° < \varepsilon < 0°$, and right-hand elliptical by $0° < \varepsilon < +45°$. The quantity $\sin(2\varepsilon)$ conveniently normalizes this range: $\sin(2\varepsilon) = -1$ is left-hand circular, $\sin(2\varepsilon) = 0$ is linear, and $\sin(2\varepsilon) = +1$ is right-hand circular polarization. Details on retrieving $\sin(2\varepsilon)$ from the data are given in the Appendix. Once we have the angle ε, we can get the aspect ratio as $\tan(\varepsilon)$. The aspect ratio is also the polarization divided by i. We can then get the angle θ (between k and B_0) by equation (9) and interpolation from the theoretical curves (see Figure 2b).

Figure 5 shows the angle θ (between k and B_0) color coded versus both time (horizontal) and frequency (vertical). The window is 256 samples wide and advances by 1/16 of its width. We condition each pixel being treated by whether its wave spectral density is above a threshold. The Stokes intensity is essentially the spectral density of the wave, resolved in our case in both frequency and time (see Appendix). Each pixel in Figure 5 is color coded as long as that pixel's Stokes intensity exceeds a threshold, equal to 10^{-3} times the maximum intensity. In other words, pixels are colored to code the angle θ only if the value of intensity I in the pixel is within three decades of the brightest pixel's intensity. Pixels with less intensity are held dark. In this
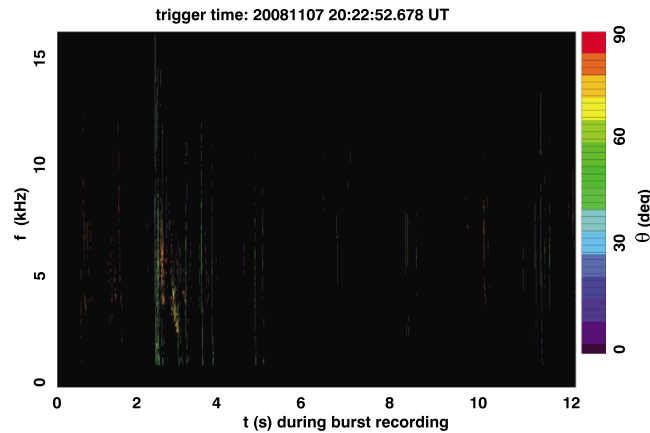
trigger time: 20081107 20:22:52.678 UT

Figure 5. Color-coded angle θ (between *k* and B_0) versus time (horizontal) and frequency (vertical) for the entire 12 s record. Each pixel is color coded only if its Stokes intensity (see Appendix) exceeds a threshold, given by 10^{-3} times the maximum intensity in the record.

manner, we indicate the angle θ only where there is significant signal. The interpolation to obtain angle θ is not done below 1 kHz, where the theoretical curves (Figure 2b) are rapidly varying. Also, the interpolation is done only for those pixels with right-hand sense of rotation; this excludes the strong carrier seen in Figure 4 above.

Figure 5 demonstrates a few quasi-distinct features in the highest-intensity-threshold data. The most common feature is broadband, weakly dispersed fractional hop whistler signatures due to lightning [*Chum et al.*, 2006; *Chum et al.*, 2009; *Jacobson et al.*, 2011; *Santolik et al.*, 2009]. This dominant broadband whistler signature is colored green, corresponding to the angle θ in the range 40–50°. A smaller portion of the whistlers are colored yellow and red, corresponding to angle θ in the range >70°. The dominant feature corresponds to the nearly vertically propagation expected for zero hop whistlers viewed in the ionosphere. The minor feature with θ > 70° is unlikely a zero hop whistler, due to the implicit large angle off of the local vertical.

A histogram of angle θ (from pixels in Figure 5) is shown in Figure 6, which indicates that there are two main features in the 12 s recording. The narrower feature is for angle θ peaking at 84–85°, indicating *k* nearly orthogonal to B_0. This feature contains fewer pixels but is very narrow. As will be made clearer in the next section, the near-orthogonal-propagating mode has much stronger dispersion, consistent with a slower group velocity as expected for θ peaking at 84–85°. The wider and more populated feature is for angle θ in the range of 40–50°. Given that the geomagnetic inclination at the satellite is −41.2°, this latter mode is consistent with *k* being nearly vertical.

Figure 7 is analogous to Figure 5 but instead indicates the inferred τ from the measured major axis rotation from the *e* axis toward the *m* axis, pixel by pixel in the same time/frequency plane used in Figure 5. The angle τ ranges from −90 to +90°, and either of those extremes is indistinguishable from the other, as the ellipse is reflection symmetric. Pixels are left dark for |sin(2 ε)| > 0.95, because the major axis rotation of a near-circular shape is

nearly impossible to infer (and is nearly meaningless anyway). Therefore, the only colored pixels in Figure 7 correspond to noncircular polarization.
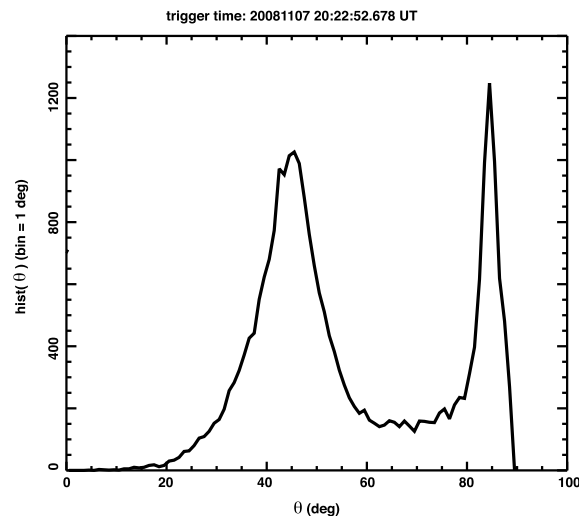
Figure 8 graphs a distribution of major axis rotation τ from the colored pixels in Figure 7. The radial direction is the count of pixels in each 1° wide bin of τ. The magnetic east zonal direction is to the right, while the meridional direction is vertical. The summation includes only pixels with 12 kHz > *f* > 1 kHz, so as to exclude both the proton whistler and the powerful man-made carrier above 12 kHz. The elongated shape of the distribution is not the polarization ellipse. Rather, the elongated shape of the distribution in Figure 8 is due to the narrow range of the major axis orientation. Discrete 30° reference angles are shown in dashed lines, with zonal in solid red and meridional in blue. The distribution peaks nearly
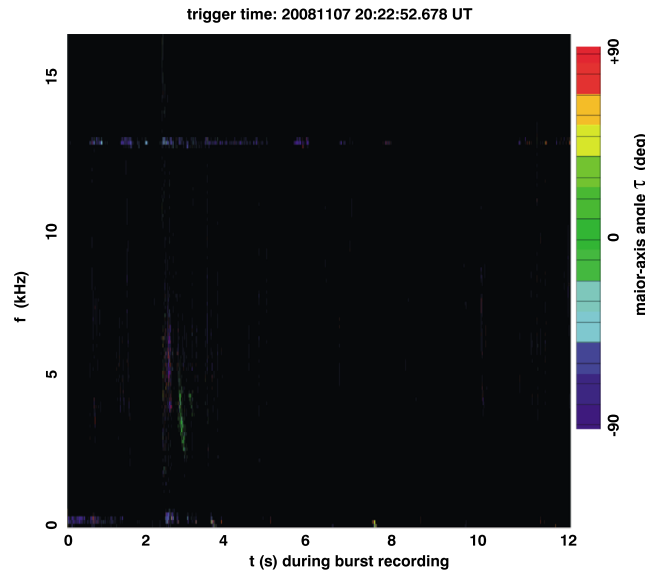
trigger time: 20081107 20:22:52.678 UT

Figure 6. Histogram of the angle θ (between *k* and B_0) for the entire 12 s record, based on the pixels in Figure 5.

Figure 7. Major axis tilt τ in the plane normal to B_0 versus time (horizontal) and frequency (vertical) for the entire 12 s record. The tilt ranges from −90 to +90°. Each pixel is color coded only if its Stokes intensity (see Appendix) exceeds a threshold, given by 10^{-3}, relative to the pixel with maximum brightness. Pixels whose intensity is subthreshold are left black. Also, pixels are colored only for $|\sin(2\varepsilon)| < 0.9$, in order to avoid the circular polarization limit in which tilt is meaningless.

(though not quite) in the meridian. That is, the major axis is nearly in the meridian, so the minor axis is nearly zonal. This is consistent with the wave vector k lying in the magnetic meridian: We know from equation (8) that the ellipse major axis is aligned with the k, B_0 plane's intersection with the plane normal to B_0. For k lying in the meridian, then the k, B_0 plane is automatically the meridian too, leading to the near alignment of the major axis with the meridian. In addition to the dominant in-meridian peak, there is also a weak feature in the distribution almost normal to the meridian. This weaker, zonal-oriented alignment arises from the minor green-colored pixels in Figure 7.

3.3. Details of Whistlers at Shorter Time Scale

We now examine a half-second-duration window, from $t = 0.25$ s to $t = 0.75$ s within the 12 s duration record. For these short windows, we automatically "dechirp," that is compensate for the whistler dispersion of the mode present and having the highest power in the short window [*Jacobson et al.*, 2011]. Figure 9a shows the angle θ (between k and B_0), for three decades of dynamic range in the Stokes intensity I (see Appendix), similarly to Figure 5a above. The green-colored features are the less eccentric, which are the weaker feature in this particular half-second window. The red/yellow featu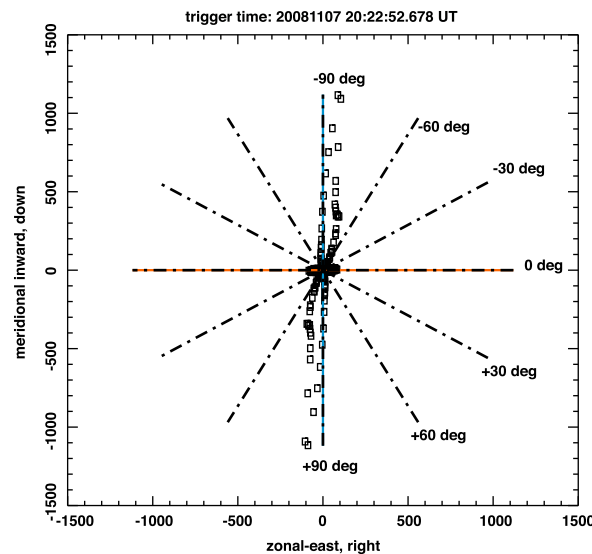res are the more eccentrically polarized waves, which dominate the intensity in this half-second window. The more eccentrically polarized feature happens to be more dispersed than is the less eccentric feature. Because of this, the green features are artificially inverse chirped in Figure 9a; that is, they have been overcompensated for dispersion. What had appeared in Figures 4 and 5 to be only a dim blur now is revealed to be a complex series of quasi-discrete pulses. There is also a weak and fragmented swarm of extremely dispersed noise, between 2 and 4 kHz, but this noise provides only a minority of the overall power in this window.

Figure 8. Polar histogram of major axis tilt angle τ in the plane normal to B_0, from the pixels in Figure 7. Discrete reference lines of τ in 30° steps are shown as dashed lines. Pixels are counted in the histogram only for frequencies in the range of 1–12 kHz and only for $|\sin(2\varepsilon)| < 0.9$, in order to avoid the circularly polarized features in which major axis tilt is meaningless.

Figure 9b histograms the angle θ (between k and B_0), for the band 1–12 kHz. Unlike the entire record (in Figure 6), this short window's strongest feature is the peak at θ ~ 85°, corresponding to the red feature in Figure 9a. The weaker feature in Figure 9b is near θ ~ 45–50°, corresponding to the green pixels in Figure 9a.

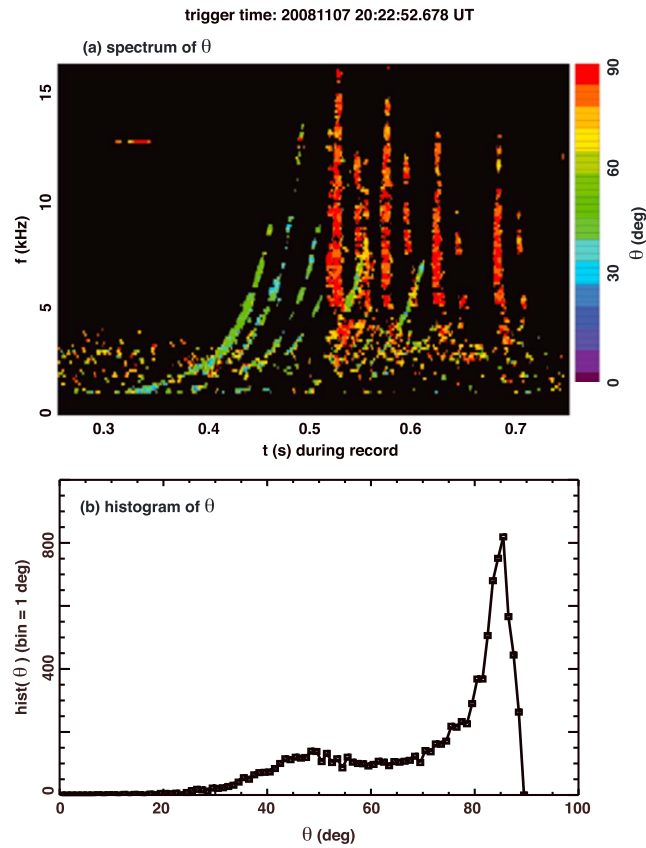Figure 10a shows the major axis tilt angle τ for the same short record as in Figure 9a. Pixels

Figure 9. (a) Color-coded angle θ (between k and B_0) versus time (horizontal) and frequency (vertical) for the first half-second short window in the record. Each pixel is color coded only if its Stokes intensity (see Appendix) exceeds a threshold, given by 10^{-3} relative to the pixel with maximum brightness. Pixels whose intensity is subthreshold are left black. (b) Distribution of angle θ (between k and B_0) versus $\sin(2\varepsilon)$ for the first half-second short window of the record, based on the pixels in Figure 9a.

are colored only for $|\sin(2\varepsilon)| < 0.95$, so nearly circular polarization features are missing. The magenta color indicates the $\tau = -90°$ extreme, while the red color indicates the $\tau = +90°$ extreme. As noted earlier, these two extremes are equivalent, due to the symmetry of an ellipse. Most of the pixels are contained in the lobe for which $\tau \sim -80°$, which is nearly but not quite in the meridian. This includes both of the peaks in the angle θ noted in Figure 9.

Figure 10b shows a histogram of pixel τ in the band 1–12 kHz. The result indicates that the major axis is nearly in the magnetic meridian, as we had seen is the case with the overall record (see Figure 8). Note that there is a minor feature aligned zonally in Figure 10b, corresponding to the green pixels in Figure 10a.

4. Discussion

We have shown (equation (8)) how the wave nonzero electric field parallel to the wave vector k, plus the requirement that the wave E must be normal to the background geomagnetic field B_0, affects the polarization ellipse in the plane normal to B_0. Prior to analyzing an epoch of data, we do not know anything about the orientation of k, so although the plane normal to k is conventionally used to characterize the polarization ellipse, we must initially use the plane

normal to B_0, the orientation of which we know. Equation (8) allows us to transfer the polarization ellipse that we measure in the plane normal to B_0 to the polarization ellipse in the plane normal to k. The dispersion relation and the polarization following from that relation then provide an inference of the wave vector k. The wave vector azimuth τ (around B_0) inferred in this way is ambiguous by modulo 180°, and the wave vector polar angle θ is ambiguous with 180°−θ.

In the present case, whether for the entire 12 s record (Figures 5–8) or for an individual 0.5 s record (Figures 9 and 10), for the eccentrically right elliptical wave feature, we infer a polar angle θ = 85° (or ambiguously, 180–84° = 95°) and an azimuth nearly meridional inward ($\tau \sim -80°$). In lieu of at least a fourth recorded wave component (namely, a component of wave B_0), we cannot resolve that fourfold ambiguity. Note however that this ambiguity does not affect either the index of refraction or the polarization [*Gurnett et al.*, 1965].

A future article will use a raytracing model to perform a backward raytrace [along the lines of, e.g., *Chum et al.*, 2009, section 3] from the satellite, using the fourfold ambiguous wave vector k to launch the ray with each of the four possible vector values of k. Without any knowledge of wave vector, the raytrace could not be initiated. However, even the ambiguous wave vector specification we use should allow reasonable comparison with other data: The raypath thus calculated will predict the longitude and the latitude of an entry point (from the Earth-ionosphere waveguide into the ionosphere), and the signal delay will then be compared with that predicted by stroke location/timing data from contemporary lightning monitoring

trigger time: 20081107 20:22:52.678 UT
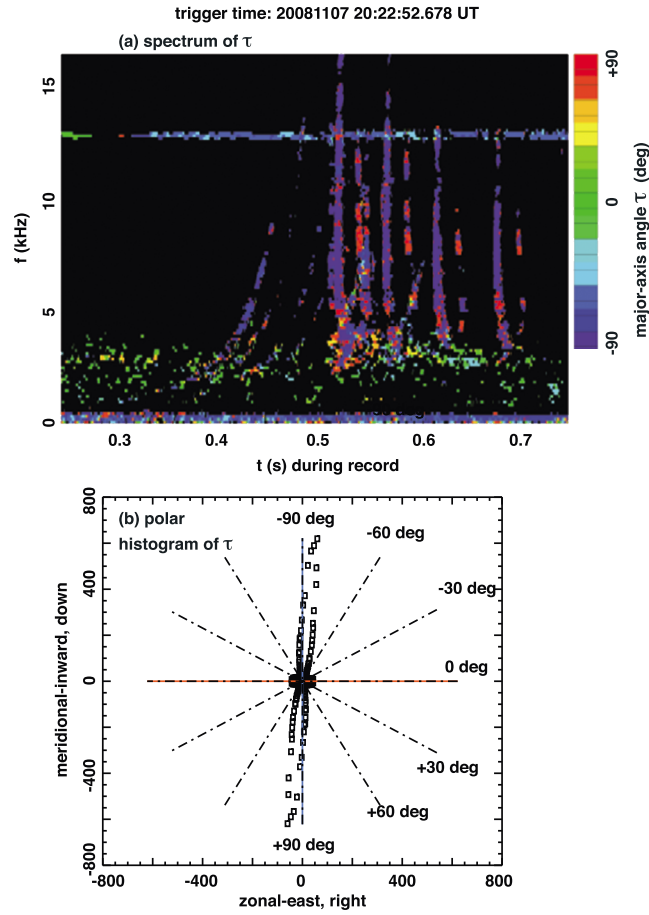
(a) spectrum of τ

Figure 10. (a) Major axis tilt τ in the plane normal to B_0 versus time (horizontal) and frequency (vertical) for the first half-second window in the record. The tilt ranges from −90 to +90°. Each pixel is color coded only if its Stokes intensity (see Appendix) exceeds a threshold, given by 10^{-3} relative to the pixel with maximum brightness. Pixels whose intensity is subthreshold are left black. Also, pixels are colored only for $|\sin(2\varepsilon)| < 0.9$, in order to avoid the circular polarization limit in which tilt is meaningless. (b) Polar histogram of major axis tilt angle τ in the plane normal to B_0, from the pixels in Figure 10a. Discrete reference lines of τ in 30° steps are shown as dashed lines. Pixels are counted in the histogram only for $|\sin(2\varepsilon)| < 0.9$, in order to avoid the circularly polarized features in which major axis tilt is meaningless.

systems, e.g., World Wide Lighting Location Network (WWLLN) [*Hutchins et al.*, 2012, 2013; *Lay et al.*, 2004; *Rodger et al.*, 2005, 2006]. If past experience [*Jacobson et al.*, 2011] with WWLLN- C/NOFS comparison is any guide, reconciling the measured time of arrival at C/NOFS with the time of arrival predicted by WWLLN will be able to discriminate between the ambiguities in wave vector.

Appendix A: Polarimetry Method

A1. Geometry

The C/NOFS satellite [*de La Beaujardiere*, 2004] carries the Vector Electric Field Instrument payload [*Pfaff et al.*, 2010]. The C/NOFS orbit is very low inclination (~13°) and slightly elliptical (perigee~400 km, apogee~850 km). The VEFI contains three orthogonal antenna pairs to measure the electric field, from DC through very low frequency. Each antenna pair extends ~20 m tip to tip. The satellite is attitude stabilized in its orbital plane and does not spin. The C/NOFS satellite orbital plane contains the antenna pairs 3, 4 and 5, 6. The third antenna pair (1, 2) is normal to the orbital plane. The orientations of electric fields $E_{3, 4}$ and $E_{5, 6}$ are shown in red in Figure A1a, along with the spacecraft coordinates (x_{sc}, y_{sc}, and z_{sc}) in solid black. The ram direction is along x_{sc}, while the nadir is along z_{sc}. The y_{sc} axis points toward the nominal

south flank, and the antenna pair 1, 2 gives $E_{1, 2}$ along the y_{sc} axis. The 3, 4 and 5, 6 antenna pairs are offset by +/−45° from the nadir, so the electric field components in the spacecraft coordinates are

$$E_{xsc} = \cos(45°)(E_{56} - E_{34}). \tag{A1a}$$

$$E_{zsc} = \cos(45°)(E_{56} + E_{34}). \tag{A1b}$$

$$E_{ysc} = E_{12}. \tag{A1c}$$

The plane normal to B_0 intersects the plane z_{sc}, x_{sc} in a straight line, shown as the direction x_u in Figure A1a. The "u" coordinate system is defined via a rotation, by angle α, around the y_{sc} axis. The (x_u, y_u, and z_u) components of E are

$$E_{xu} = E_{xsc}\cos(\alpha) - E_{zsc}\sin(\alpha). \tag{A2a}$$

$$E_{zu} = E_{zsc}\cos(\alpha) + E_{xsc}\sin(\alpha). \tag{A2b}$$

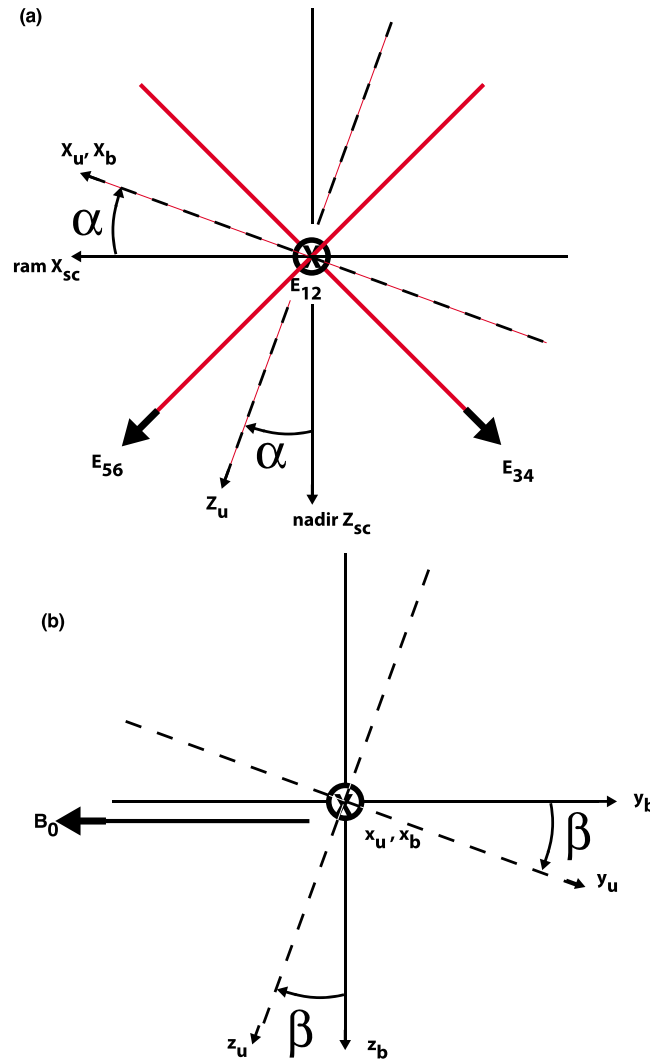$$E_{yu} = E_{ysc} = E_{12}. \tag{A2c}$$

Figure A1. (a) Orbital plane of C/NOFS, showing VEFI antenna axes $E_{3, 4}$ and $E_{5, 6}$ in red in that plane. The third antenna axis, $E_{1, 2}$, is normal to the plane. The spacecraft coordinates are x_{sc} (ramward), z_{sc} (nadirward), and y_{sc} (into page). The plane normal to the geomagnetic field B_0 intersects the orbital plane along an axis x_u. The pair of coordinates (x_u and z_u) are rotated clockwise around y_{sc} by an angle α, relative to the spacecraft coordinates (x_{sc} and z_{sc}). In the coordinates tied to $\boldsymbol{B_0}$, the x_b axis coincides with x_u. (b) Definition of the coordinates (x_b, y_b, and z_b) tied to B_0. The axis x_b coincides with x_u and is into the page. Both x_b and x_u are along the intersection of the plane normal to B_0 and the orbital plane. The axis y_b is antiparallel to B_0. The axes (y_b and z_b) are derived from (y_u and z_u) by a counterclockwise rotation through angle β.

Finally, let us define the coordinates (x_b, y_b, and z_b), formed from the (x_u, y_u, and z_u) coordinates via a rotation through angle β about the x_u axis, such that B_0 is along the $-y_b$ direction, as shown in Figure A1b. We have

$$E_{xb} = E_{xu}. \tag{A3a}$$

$$E_{yb} = E_{yu}\cos(\beta) - E_{zu}\sin(\beta). \tag{A3b}$$

$$E_{zb} = E_{zu}\cos(\beta) + E_{yu}\sin(\beta). \tag{A3c}$$

Equations (A1)–(A3) allow us to construct the components $E_{xb}, E_{yb}, and E_{zb}$. on the recorded antenna pair fields $E_{1, 2}, E_{3, 4}, and E_{5, 6}$. The wave polarization is retrieved from the components $E_{xb}, E_{yb}, and E_{zb}$. cause we expect the magnetic field direction to control the polarization. The angles α and β in equations (A2) and (A3) are obtained by combining the satellite ephemeris and the tenth-order IGRF magnetic field specification.

We now transform to axes that are more natural in the geomagnetic context. We rotate the two coordinates (x_b and z_b) about $-y_b$, so as to get two familiar axes in the plane normal to B_0: Magnetic zonal eastward e, normal to the magnetic meridian surface, and magnetic meridional inward m, within the magnetic meridian surface. This is shown in Figure A2, which diagrams the plane whose normal is B_0. The rotation from coordinates (x_b and z_b) to coordinates (e and m) is by an angle ψ around $-y_b$. The axes (e and m) are shown by heavy dashed lines, while the axes (x_b and z_b) are shown in solid lines.

A2. Relationship to Wave Vector k

Figure 1 in this article's main body shows the "k, B_0 plane," containing both k and B_0. Normal to this plane, into the page, we shall call the x_v axis. This x_v axis is the intersection of the plane normal to B_0 and the plane normal to k. The magnetic field B_0 is along the $-y_v$ direction (coinciding with $-y_b$ direction). The axis z_v lies in the k, B_0 plane and is normal to the y_v axis, which also lies in the k, B_0 plane. Figure A2 diagrams the plane normal to B_0, and the (x_v, y_v, and z_v) axes are shown with light dashed lines. These axes are rotated from the (e, m, $-y_b$) axes by an angle η around $-y_b$. If k is parallel to B_0, there is no breaking of symmetry about B_0, and the polarization in the plane normal to B_0 must be circular. If on the other hand k is not parallel to B_0, i.e., is
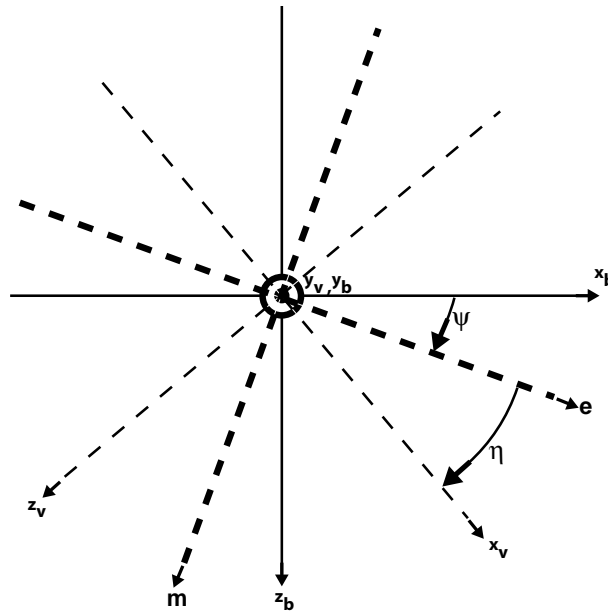
Figure A2. View of the plane normal to B_0, showing transformation of coordinates (x_b, y_b, and z_b) into (e, y_b, and m) via a clockwise rotation ψ around y_b, where e is directed magnetic zonal eastward and m is directed magnetic meridional inward. Also shown is the transformation from (e, y_b, and m) to (x_v, y_v, and z_v) via a clockwise rotation η around y_b. B_0 is directed into the page.

nonzero in Figure 1, then the symmetry about B_0 is broken, and we conclude that each principal axis of the polarization ellipse must lie along either the x_v axis or the z_v axis. The azimuth of k about B_0 controls the principal axes of the polarization, although it is still undetermined from this asymmetry alone whether the major or the minor axis is associated with x_v. That will be determined by (a) the behavior of the polarization in the plane normal to k, (b) by the transformation from that plane to the plane normal to B_0, and (c) by the constraint that E must vanish along B_0.

A3. Polarization Angles

The polarization will be retrieved from the data in the plane normal to B_0, with B_0 directed along $-y_b$ axis. Thus, we use a right-hand system (e, m, and $-y_b$), with e and m in the plane normal to B_0.

The formal description of the polarization state of a wavefield is based entirely on the 1852 article by G. G. Stokes, then a Fellow of Pembroke College and the Lucasian Professor of Mathematics at the University of Cambridge [*Stokes*, 1852]. The present use of his formalism with VEFI is no real advance over the original article of 1852, except for the speed with which computers can apply Professor Stokes' formulation to copious data. Without the loss of generality, the electric field of a single-wave mode will be elliptically polarized in the plane normal to the magnetic field.

The polarization ellipse in the plane normal to B_0 is shown in Figure A3. The axis y_b is out of the page, so B_0 and $-y_b$ are into the page. The tilt of the major axis with respect to e is τ and is figured positive clockwise. The domain of τ is from -90 to $+90°$. Figure A3 shows two cases: (a) with the ellipse major axis along x_v and (b) with the ellipse major axis along z_v. For case 1, the major axis tilt τ within the domain -90 to $+90°$ is equal to η, while for case 2, the major axis points into the upper right part of the domain -90 to $+90°$, which counts as negative tilt: $\tau = \eta -90°$.

The handedness of the polarization is defined with respect to the right-hand coordinate system (e, m, and $-y_b$). The elliptical polarization is characterized by two angles [*Stokes*, 1852]. The angle ε controls the aspect ratio (minor axis, major axis) of the ellipse: aspect ratio $= \tan(\varepsilon)$. The angle ε can take values only from $-45°$ (left-hand circular) to $+45°$ (right-hand circular). Linear polarization is given by $\varepsilon = 0°$, left-hand elliptical by $-45° < \varepsilon < 0°$ and right-hand elliptical by $0° < \varepsilon < +45°$. The other Stokes-derived angle, τ, gives the rotation of the major axis of the ellipse from e toward m and is in the range $-$of $90°$ to $+90°$. Since an ellipse is symmetric about either principal axis, τ is equivalent to $\tau + 180°$.

A4. Stokes Parameters

Assuming that E is normal to B_0, we express the electric field in the plane normal to B_0 as

$$E_e = E_1 sin(\omega t - \delta_e). \tag{A4a}$$

$$E_m = E_2 sin(\omega t - \delta_m). \tag{A4b}$$

Defining the intensity as
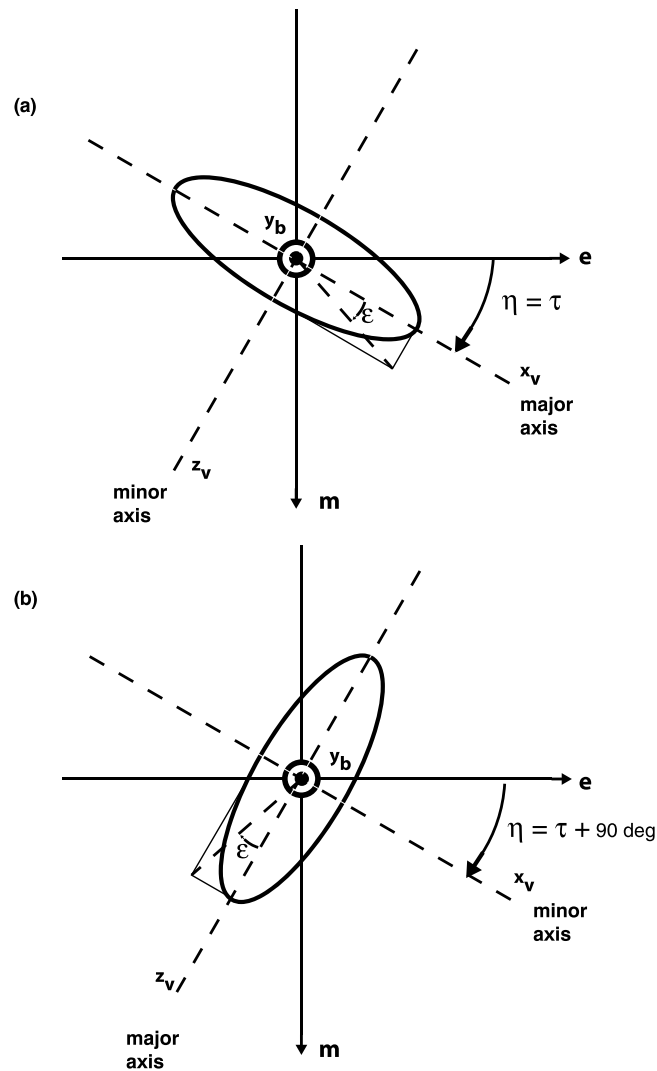
$$I \stackrel{\text{def}}{=} E_1^2 + E_2^2. \tag{A5}$$

Figure A3. View of the plane normal to $\boldsymbol{B}_0$, showing the polarization in this plane relative to the e (magnetic zonal eastward) and m (magnetic meridional inward) axes. B_0 is into the page. Two cases are shown, because τ, the clockwise angle of the major axis from the e direction toward the m direction, runs from $-90°$ to $+90°$: (a) For positive τ, x_v coincides with the major axis. (b) For negative τ, x_v coincides with the minor axis. In each case, the angle ε controls the minor:major axis = ratio tan(ε).

we can relate the observables E_1 and E_2 and the phase difference δ_e–δ_m to derive the polarization angles using the classic Stokes relations [*Shao and Jacobson*, 2001]:

$$Q \stackrel{\text{def}}{=} E_1^2 \;-\; E_2^2$$
$$= I \cdot \cos(2\epsilon) \cdot \cos(2\tau). \qquad (A6)$$

$$U \stackrel{\text{def}}{=} 2E_1 E_2 \cos(\delta_e - \delta_m)$$
$$= I \cdot \cos(2\epsilon) \cdot \sin(2\tau). \qquad (A7)$$

$$V \stackrel{\text{def}}{=} 2E_1 E_2 \sin(\delta_e - \delta_m)$$
$$= I \cdot \sin(2\epsilon). \qquad (A8)$$

For a single-wave mode, the four Stokes parameters obey

$$I^2 = Q^2 + U^2 + V^2. \qquad (A9)$$

There are three (and only three) independent parameters describing the polarization state of a single-wave mode. These independent parameters can be chosen either as (a) E_1, E_2, and (δ_e–δ_m) or as (b) I, τ, and ε. Equations (A6)–(A8) describe the relationship between the two alternative parameter sets. We stress that the interpretation of polarization depends on there being only a single wave present during the analysis. The presence of multiple waves, each with its own (and differing) polarization, will confound the overall polarization analysis. The latter situation is called "random polarization." In that case, the various angles observed, whether δ_e and δ_m or τ and ε, are ill determined (and meaningless). The discussion of Figures 9 and 10 above confirms that the majority of the wideband pulses are narrow and discrete, consistent with there being only a single-wave mode affecting a polarimetry pixel.

We also stress that polarimetry demands high-fidelity signal recording, i.e., accurate and unbiased measurements of the relative power and phase on the three antennas. We select data to ensure this by testing the underlying assumption of this work, that the wave electric field $\boldsymbol{E}$ is orthogonal to the background geomagnetic field B_0. Prior to attempting polarimetry on any particular three-channel recording of E, we test for this orthogonality. The entire record is Fourier transformed and high passed >1 kHz; we find that this is a good protection against the confounding effects of unbalanced plasma interactions with the two ball electrodes of an antenna pair. The complex Fourier coefficients for each antenna are then transformed into B_0-based coordinates (see equations (A2) and (A3)), and we evaluate the ratio of the mean square electric field parallel to B_0, over the mean square electric field perpendicular to B_0. For the data recording used in this article, that ratio is 1.7×10^{-3}. This is quite a typical level when (a) there is no electrical interference from the C/NOFS attitude control system and (b) when there is relatively slowly varying ion density. Regarding the latter, the relative Langmuir probe incorporated in VEFI permits us to monitor for density irregularities.

If C/NOFS is within an occasional "plasma bubble" depletion, we find extremely noisy fine-scale density structure manifested as incoherent signals at and above the lower hybrid frequency [*Bell and Ngo*, 1988, 1990]. Presumably, there is a cascade downward in scale to the antenna scale (20 m), causing the antenna differential measurement to transition from being a point measurement of E to starting to be a voltage interferometer. In that case, we cannot expect the flawed "electric field vector" to remain perpendicular to B_0. We find that about 20–30% of the archived recordings have sufficient density irregularities to promote a parallel/perpendicular ratio exceeding 0.01, which is our operational upper limit for polarimetry.

References

Barrington, R. E., and J. S. Belrose (1963), Preliminary results from the Very-Low Frequency receiver aboard Canada's Alouette satellite, *Nature*, *198*, 651–656.

Bell, T. F., and H. D. Ngo (1988), Electrostatic waves stimulated by coherent VLF signals propagating in and near the inner radiation belt, *J. Geophys. Res.*, *93*(A4), 2599–2618.

Bell, T. F., and H. D. Ngo (1990), Electrostatic lower hybrid waves excited by electromagnetic whistler mode waves scattering from planar magnetic-field-aligned plasma density irregularities, *J. Geophys. Res.*, *95*(A1), 149–172.

Berthelier, J. J., et al. (2006), ICE, the electric field experiment on DEMETER, *Planet. Space Sci.*, *54*, 456–471, doi:10.1016/j.pss.2005.10.016.

Carpenter, D. L., N. Dunckel, and J. F. Walkup (1964), A new Very Low Frequency phenomenon: Whistlers trapped below the protonosphere, *J. Geophys. Res.*, *69*(23), 5009–5017.

Chum, J., F. Jiricek, O. Santolik, M. Parrot, G. Diendorfer, and J. Fiser (2006), Assigning the causative lightning to the whistlers observed on satellites, *Ann. Geophys.*, *24*, 2921–2926.

Chum, J., O. Santolik, and M. Parrot (2009), Analysis of subprotonospheric whistlers observed by DEMETER: A case study, *J. Geophys. Res.*, *114*, A02307, doi:10.1029/2008JA013585.

Cummer, S. A. (2000), Modeling electromagnetic propagation in the Earth-ionosphere waveguide, *IEEE Trans. Antennas Propag.*, *48*(9), 1420–1429.

de La Beaujardiere, O. (2004), C/NOFS: A mission to forecast scintillations, *J. Atmos. Sol. Terr. Phys.*, *66*, 1537–1591, doi:10.1016/j.jastp.2004.07.030.

Gurnett, D. A., S. D. Shawhan, N. M. Brice, and R. L. Smith (1965), Ion cyclotron whistlers, *J. Geophys. Res.*, *70*(7), 1665–1668.

Heelis, R. A., W. R. Coley, A. G. Burrell, M. R. Hairston, G. D. Earle, M. D. Perdue, R. A. Power, L. L. Harmon, B. J. Holt, and C. R. Lippincott (2009), Behavior of the O+/H + transition height during the extreme solar minimum of 2008, *Geophys. Res. Lett.*, *36*, L00C03, doi:10.1029/2009GL038652.

Helliwell, R. A. (2006), *Whistlers and Related Ionospheric Phenomena*, pp. 349, Dover Publications, Mineola, New York.

Hutchins, M. L., R. H. Holtzworth, C. J. Rodger, and J. B. Brundell (2012), Far-field power of lightning strokes as measured by the World Wide Lightning Location Network, *J. Atmos. Oceanic Technol.*, *29*, 1102–1110, doi:10.1175/JTECH-D-11-00174.

Hutchins, M. L., A. R. Jacobson, R. H. Holzworth, and J. B. Brundell (2013), Azimuthal dependence of VLF propagation, *J. Geophys. Res. Space Physics*, *118*, 5808–5812, doi:10.1002/jgra.50533.

Jacobson, A. R., R. H. Holzworth, R. F. Pfaff, and M. P. McCarthy (2011), Study of oblique whistlers in the low-latitude ionosphere, jointly with the C/NOFS satellite and the World-Wide Lightning Location Network, *Ann. Geophys.*, *29*, 851–863, doi:10.5194/angeo-29-851-2011.

Lay, E. H., R. H. Holzworth, C. J. Rodger, J. N. Thomas, O. Pinto, and R. L. Dowden (2004), WWLL global lightning detection system: Regional validation study in Brazil, *Geophys. Res. Lett.*, *31*, L03102, doi:10.1029/2003GL018882.

Means, J. D. (1972), Use of the three-dimensional covariance matrix in analyzing the polarization properties of plane waves, *J. Geophys. Res.*, *77*(28), 5551–5559.

Parrot, M., J. J. Berthelier, J. P. Lebreton, R. Treumann, and J. L. Rauch (2008), DEMETER observations of EM emissions related to thunderstorms, *Space Sci. Rev.*, *137*, 511–519, doi:10.1007/s11214-008-9347-y.

Pfaff, R., et al. (2010), Observations of DC electric fields in the low-latitude ionosphere and their variations with local time, longitude, and plasma density during extreme solar minimum, *J. Geophys. Res.*, *115*, A12324, doi:10.1029/2010JA016023.

Rodger, C. J., J. B. Brundell, and R. L. Dowden (2005), Location accuracy of VLF World Wide Lightning Location (WWLL) network: Post-algorithm upgrade, *Ann. Geophys.*, *23*, 277–290.

Rodger, C. J., S. Werner, J. Brundell, E. H. Lay, N. R. Thomson, R. H. Holzworth, and R. L. Dowden (2006), Detection efficiency of the VLF World-Wide Lightning Location Network (WWLLN): Initial case study, *Ann. Geophys.*, *24*, 3197–3214.

Santolik, O., M. Parrot, and F. Lefeuvre (2003), Singular value decomposition methods for wave propagation analysis, *Radio Sci.*, *38*(1), 1010, doi:10.1029/2000RS002523.

Santolik, O., M. Parrot, U. S. Inan, D. Buresova, D. A. Gurnett, and J. Chum (2009), Propagation of unducted whistlers from their source lightning: A case study, *J. Geophys. Res.*, *114*, A03212, doi:10.1029/2008JA013776.

Shao, X.-M., and A. R. Jacobson (2001), Polarization observations of broadband VHF signals by the FORTE satellite, *Radio Sci.*, *36*(6), 1573–1589.

Smith, R. L. (1965), An explanation of subprotonospheric whistlers, *J. Geophys. Res.*, *69*(23), 5019–5021.

Stix, T. H. (1962), *The Theory of Plasma Waves*, McGraw Hill Book Company, New York.

Stokes, G. G. (1852), On the composition and resolution of streams of polarized light from different sources, *Trans. Cambridge Phil. Soc.*, *9*(III), 399–416.